ULTRASONIC IMAGING 16, 1—18 (1994)

IMPROVED DETECTABILITY WITH BLOCKED ELEMENT COMPENSATION

Pai-Chi Li and M. O'Donnell

Electrical Engineering and Computer Science Department
University of Michigan
Ann Arbor, MI 48109-2122

The inability of diagnostic ultrasound to detect low contrast lesions deep inside the body has limited its success in cancer diagnosis. To enhance low contrast detectability, two-dimensional, very large arrays (VLA's) providing greatly improved spatial resolution have been proposed. Due to discontinuous acoustic windows into the body, however, a significant fraction of such an array might be blocked resulting in degraded detectability in clinical situations. To compensate for this degradation, an object dependent method utilizing multiple receive beams has been proposed and shown to effectively reduce undesired beamforming artifacts. To further explore the method's capabilities, simulations have been done quantifying improvements in contrast resolution. Using the contrast-to-noise ratio (CNR) as a performance measure, results show that low contrast detectability is determined by sidelobe energy in the point spread function if the total aperture size is not reduced. Moreover, contrast resolution can be restored using the object dependent method if the number of blocked elements is not very significant. If the number of blocked elements is large, however, the method breaks down and performance improvements are minimal.

Key words: Blocked element compensation; contrast resolution; detectability; multiple receive beamforming; very large array.

1 INTRODUCTION

Detecting low contrast lesions embedded in similar backgrounds is an essential task of all medical imaging modalities. In diagnostic ultrasound, it has been shown that one of the primary limitations on low contrast detectability is image speckle [1]. Speckle results from coherent interference of scatterers (i.e., linear summation by the transducer of echoes from scatterers) in a finite resolution volume. Its granular structure masks image details and therefore limits detectability. Several techniques, such as frequency and spatial compounding, have long been explored to reduce speckle variance [2–6]. The improved contrast resolution of these methods, however, is gained at the price of decreased spatial resolution. To improve *both* spatial and contrast resolution, the imaging voxel must be reduced. In other words, only large size apertures can greatly improve the detectability of small objects in tissue.

Several types of large, two-dimensional arrays have been proposed. First, fully sampled two-dimensional arrays capable of steering in both azimuth and elevation can be

0161-7346/94 $6.00

used for real-time, three-dimensional imaging [7, 8]. The major drawback, however, is the hardware complexity and complicated interconnect problem created by the large number of channels. Second, two-dimensional sparse arrays have been proposed to reduce the complexity of fully sampled two-dimensional arrays while avoiding unwanted grating lobes [9]. Average sidelobe levels, however, increase as the number of elements decreases. Finally, anisotropic arrays have been investigated to reduce the number of channels by undersampling the aperture in elevation. Such arrays are also referred to as 1.5 dimensional arrays [10]. Anisotropic arrays are not suitable for real-time, three-dimensional imaging due to the limitation of beam steering in the elevational direction. Nevertheless, they can be used to correct for beamforming artifacts associated with a large aperture size and greatly improve image quality of two-dimensional images.

There are two major problems associated with large arrays. One is phase aberration due to spatial inhomogeneities in the propagation medium [11–16]. Adaptive imaging systems using anisotropic arrays have been proposed to overcome the lack of phase coherence over large areas of the body [10]. On the other hand, due to the discontinuous acoustic windows into the body, a significant portion of the array is likely to be blocked in clinical situations if the aperture size is large. This results in the second major problem: blocked elements.

Blocked elements receive abnormal echo energy and therefore can be easily detected using the receive amplitude distribution across the aperture as a function of transmit direction and range. To minimize image artifacts, blocked elements should not contribute to either transmit or receive beamforming (i.e., they should be turned off). Corrupted beam patterns can be modeled as a superposition of two patterns, one resulting from the full array and the other from blocked (missing) elements driven with a negative signal. In general, blocked elements produce higher sidelobes in the point spread function. Additionally, a wider mainlobe results if blocked elements are located at the array edge, i.e., if the effective aperture size is reduced. In this paper, we will only concentrate on situations maintaining total aperture size in the presence of blocked elements.

Unfortunately, undesired artifacts resulting from blocked elements cannot be removed by compounding techniques since these methods do not reduce sidelobes. Therefore, enhancement of low contrast detectability using VLA's cannot be achieved unless a proper compensation algorithm for blocked element artifacts is applied. A method of overcoming beamforming artifacts in the presence of blocked elements has been described in [17]. This method uses multiple receive beams to estimate and remove undesired sidelobe contributions for each transmit beam of a sector scan in the presence of blocked elements. In this paper, we quantify improvements in detectability resulting from compensation. In particular, we investigate the role of compensation in contrast resolution for speckle generating objects.

In the next section, we study the factors affecting contrast resolution based on the statistics of integrated speckle patterns [19–23]. Degradation in contrast resolution due to blocked array elements is discussed in section 3. An object dependent compensation algorithm is briefly described in section 4 [17]. Note that although the blocked element problem is more pronounced in two-dimensional arrays, one-dimensional structures will be used exclusively throughout this paper for simplicity. Nevertheless, it is clear that the same principles apply to both one- and two-dimensional cases as noted in [17]. Performance of the compensation algorithm on low contrast detectability is presented in section 5.

2 DETECTABILITY

Detectability of a lesion in a noisy background is determined by local contrast and the statistics of the system [18]. Local contrast, defined as the ratio of the intensity variation

to the averaged background intensity, can be artificially enhanced, e.g., by remapping gray levels of the envelope. Noise characteristics, on the other hand, inherently limit detectability. To detect a finite lesion, statistics of averaged signals over the regions of interest (i.e., area-wise statistics) must be derived. More specifically, a contrast-to-noise ratio (CNR), defined as the ratio of the local intensity variation to the standard deviation of the averaged background intensity, is suitable for a quantitative measure of detectability. This definition is also widely used in other medical imaging modalities [18, 24]. The specific approach to derive area-wise speckle statistics presented in this section follows Goodman [19] and Smith et al [21].

If $I(x, y)$ denotes the intensity at beam direction x and range y in the image plane, the averaged signal over a target is

$$I_A = \frac{1}{S} \int \int_{-\infty}^{\infty} W(x, y) I(x, y) dx dy \quad , \tag{1}$$

where $W(x, y)$ is a weighting function describing the target and

$$S = \int \int_{-\infty}^{\infty} W(x, y) dx dy \quad . \tag{2}$$

In this paper, $W(x, y)$ is chosen to be unity inside the target and zero outside so that the constant S simply represents the target area. Assuming the point-wise first-order moment (i.e., statistical mean) of $I(x, y)$ in the target region is a constant $\langle I \rangle$, i.e., the target has a homogeneous distribution of scatterers, the mean value of the area-wise averaged signal I_A is also $\langle I \rangle$ according to the principles of superposition.

The second order moment of I_A is

$$\langle I_A^2 \rangle = \frac{1}{S^2} \int \int \int \int_{-\infty}^{\infty} W(x_1, y_1) W(x_2, y_2) \langle I(x_1, y_1) I(x_2, y_2) \rangle dx_1 dx_2 dy_1 dy_2 \quad , \tag{3}$$

where $\langle I(x_1, y_1) I(x_2, y_2) \rangle$ represents the autocorrelation function of the intensity. Assuming the speckle pattern is spatially stationary and the target area is much larger than the area where $\langle I(x_1, y_1) I(x_2, y_2) \rangle$ is appreciable, the variance of I_A has the following form [19, 21]:

$$\sigma_{I_A}^2 = \frac{1}{S} \int \int_{-\infty}^{\infty} C_I(x, y) dx dy \quad , \tag{4}$$

where $C_I(x, y)$ is the autocovariance function of $I(x, y)$.

Defining the normalized correlation cell area S_c of the target as

$$S_c \stackrel{def}{=} \int \int_{-\infty}^{\infty} \frac{C_I(x, y)}{C_I(0, 0)} dx dy \quad , \tag{5}$$

the standard deviation of the averaged signal, I_A, is

$$\sigma_{I_A} = \frac{\sigma_I}{N^{\frac{1}{2}}} \quad , \tag{6}$$

where $\sigma_I^2 (= C_I(0,0))$ is the variance of $I(x,y)$ and N represents the number of independent speckle spots in the target region defined by

$$N = \frac{S}{S_c} \quad . \tag{7}$$

From Eq. (6), we know that the standard deviation of the area-wise signal (i.e., I_A) is determined by both the standard deviation of the point-wise signal (i.e., I) and the number of speckle correlation cells.

Therefore, defining ΔI as the local intensity variation, then the CNR is

$$\Delta I \stackrel{def}{=} I_1 - I_2 \quad , \tag{8}$$

$$CNR = \frac{\langle \Delta I \rangle}{\sigma_{I_A}} = \frac{\langle \Delta I \rangle}{\sigma_I} N^{\frac{1}{2}} \quad , \tag{9}$$

where I_1 and I_2 are mean intensities of the target and the background respectively. Note that the speckle cell size, S_c, is independent of the mean intensity of the signal. A similar result to Eq. (9) is also found in nuclear magnetic resonance (NMR) imaging [24].

Since intensities of fully developed speckle have exponential statistics, speckle fluctuations can be viewed as additive noise on a logarithmic display. In a logarithmic display, the intensity of each pixel (D) and the original intensity (I) have the following relation

$$D(dB) = f(I) \stackrel{def}{=} 10 \log_{10}(\frac{I}{I_0}) \quad , \tag{10}$$

where I_0 is an arbitrary reference intensity. We can expand the function f in a Taylor series about the statistical mean (i.e., $I = < I >$) as

$$D = f(< I >) + (I - < I >) f'(< I >) + R \quad , \tag{11}$$

where R is a remainder. Ignoring R, it can be shown that the standard deviation of D (σ_D) can be approximated by [25]

$$\sigma_D^2 \approx f'(I)^2 \sigma_I^2 \tag{12}$$

$$= (\frac{10}{\ln 10})^2 \frac{\sigma_I^2}{< I >^2} \quad . \tag{13}$$

Since $\frac{<I>}{\sigma_I}$ is unity for an exponential distribution, $\sigma_D = \frac{10}{\ln 10} = 4.34$ dB. In other words, speckle noise in a logarithmically processed display is a fixed additive noise. Moreover, the variation between the target and the background on a logarithmical display is $\Delta D =$

$10\log(I_1) - 10\log(I_2) = 10\log(\frac{I_1}{I_2})$. Therefore, for a logarithmic display, a reasonable CNR for detectability based on Eq. (9) is

$$CNR = \frac{\Delta D}{\sigma_D} N^{\frac{1}{2}} \tag{14}$$

$$= \frac{10\log_{10}(\frac{I_1}{I_2})}{4.34} N^{\frac{1}{2}} \quad . \tag{15}$$

In other words, the detectability of a lesion in a speckle background is determined by two factors: (1) the ratio of mean intensities between the target and the background, respectively; and (2) the total number of speckle correlation cells in the target.

3 CONTRAST RESOLUTION WITH BLOCKED ARRAY ELEMENTS

Figure 1 shows simulated point spread functions over a 30 dB display dynamic range assuming a one-dimensional, fully sampled 64 element array with a 2.5 MHz center frequency. Note that for all the images in this paper, display dynamic range represents the thresholded signal dynamic range. These images consist of a 256 × 256 grid. The vertical axis represents the axial direction (R) and the horizontal axis the azimuth ($\sin\theta$), i.e., simulated images are in a sector format prior to scan conversion. Assuming a 10 MHz sampling rate, the 256 samples in range represent approximately a 20 mm distance. With a 0.42 mm (0.7 λ) interelement spacing, 256 samples in azimuth represent a 90° sector. The envelope of the axial response has a Gaussian shape with a 35% fractional bandwidth. The lateral response, on the other hand, is simply obtained by Fourier transforming the aperture function, i.e., a continuous wave (cw) model is assumed. Nevertheless, general principles involved in generating simulated speckle patterns still hold. The upper panel

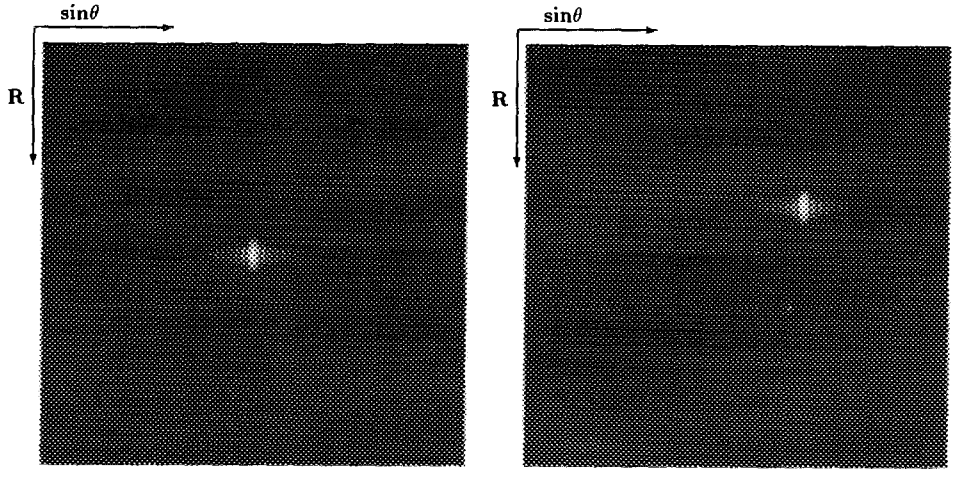

Fig. 1 Illustration of simulated point spread functions at different positions.

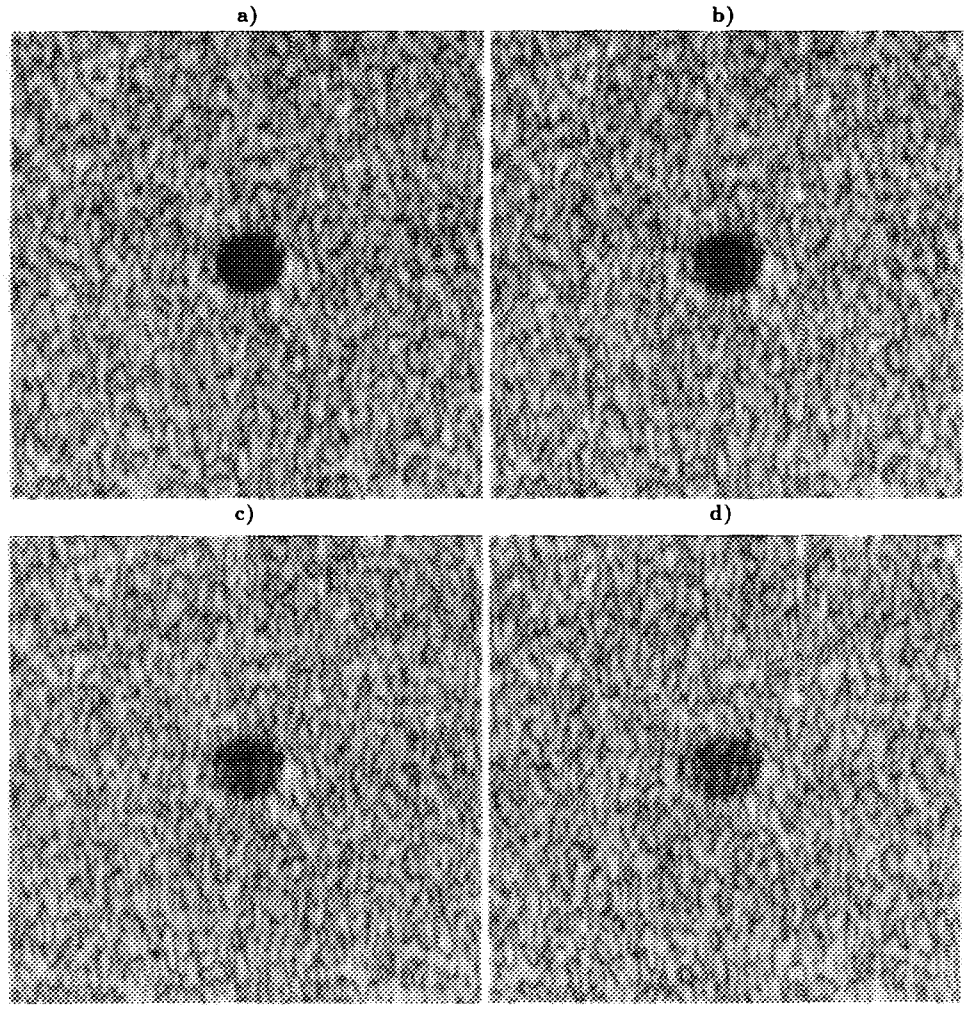

Fig. 2 Images of an anechoic region with no blocked elements (a), 8 blocked elements (b), 16 blocked elements (c) and 24 blocked elements (d).

of figure 1 shows the point spread function at the center and the lower panel shows the point spread function for a beam steered off normal at a different position. Note that in this format, dimensions of the point spread function are space invariant.

Figure 2 shows simulated images mimicking a focal lesion embedded in a uniform speckle background using the same array. All simulated lesions in this paper are centered on the array normal (i.e., center beam direction) and are circular in the R-sin θ format. In sector scan format, these lesions are approximately elliptic. To simulate speckle patterns, a two-dimensional random walk model in the complex plane is used where each step in the walk represents a received signal from a scatterer. Furthermore, the number of scatterers within a resolution cell is assumed large enough such that the phases of the echoes are uniformly distributed from $-\pi$ to π and the sum of the complex signals

has a circular Gaussian density function. Equivalently, each image pixel, i.e., the sum of the complex signals, can be characterized by a Rayleigh distributed magnitude and a uniformly distributed phase. Assuming a linear and space invariant point spread function, a speckle pattern is generated by convolving a two-way (transmit and receive), two-dimensional (axial and lateral) point spread function of the type presented in figure 1 with a target pattern consisting of 256 × 256 pixels. Each pixel in this target pattern is a complex number with statistics as described above. On the other hand, the mean of the amplitude is a constant over the entire background and a different constant over the disk. The ratio of these constants is a pre-selected local intensity variation. Since linear convolution is used, note that every pixel in the pattern is assumed in focus.

Figure 2(a) shows a full array image of an anechoic region (i.e., infinite contrast) embedded in a uniform speckle region displayed over a 40 dB dynamic range. In the original target pattern, the anechoic region has a 20 pixel radius (about 12 resolution cells). Figure 2(b) shows an image of the same target with 8 blocked elements (33-40) in the array. Since the total aperture size is not changed, the mainlobe has the same width but higher sidelobes are present because of blocked elements. Sidelobes backscattered from the background increase the averaged intensity in the disk and therefore reduce contrast.

Lower contrast is expected if the number of blocked elements increases. Figure 2(c) shows the image of the same target pattern with 16 blocked elements (17-24, 33-40) whereas figure 2(d) has 24 blocked elements (5-12, 17-24 and 33-40). Contrast is markedly reduced in these images.

As mentioned previously, detectability is determined by both local intensity variation and the number of speckle correlation cells. In figure 2, fundamental speckle patterns do not change and therefore the variation in the number of speckle correlation cells is not significant. Using Eq. (5), the change in speckle correlation cell size was quantified indicating that the change due to blocked elements is negligible. Conseqently, we conclude that sidelobe energy dominates low contrast detectability if total aperture size is not reduced in the presence of blocked elements.

Assuming that the point spread function is separable (i.e., in the focal zone), the overall lateral response is simply the convolution of a one-dimensional target pattern with the lateral response. Furthermore, assuming scatterers in the image plane are microscopic and uncorrelated with uniform mean intensity (i.e., fully developed speckle), the lateral autocorrelation function of the image is determined mainly by the autocorrelation function of the lateral response. Hence, this strong relationship between the beam pattern and the autocorrelation function suggests that mainlobe and sidelobes of the autocorrelation function of the image have characteristics similar to the mainlobe and sidelobes of the point spread function.

Figure 3 shows normalized autocorrelation functions using the average of 50 consecutive lateral lines, where the horizontal axis (beam index) indicates beams (vertical lines) in the simulated images. The solid line is with no blocked elements and the dashed line is with 40 blocked elements (5-12, 17-28, 33-44 and 53-60). Since blocked elements do not change range response [17], these correlation functions are computed only in the lateral direction. Clearly, mainlobes of the autocorrelation functions have comparable widths. On the other hand, much higher sidelobes are observed if the number of blocked elements is very significant.

4 COMPENSATION USING MULTIPLE RECEIVE BEAMS

Blocked array elements generally produce higher sidelobes in the point spread function and degrade contrast resolution. The goal of blocked element compensation, therefore,

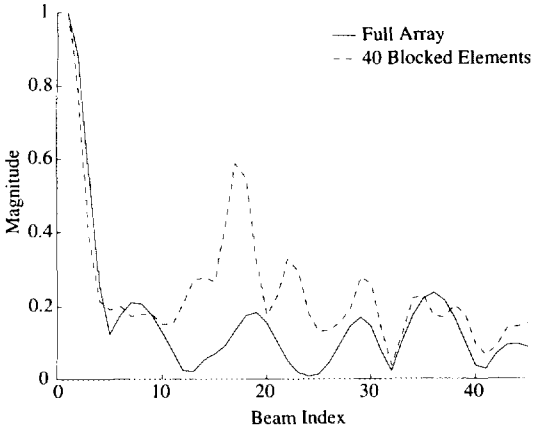

Fig. 3 Normalized autocorrelation functions in the lateral direction. Solid line is with no blocked elements and dashed line is with 40 blocked elements.

is to restore contrast resolution by removing undesired sidelobe contributions. A wider mainlobe is also produced by blocked elements if the total aperture size is reduced. Degradation in spatial resolution resulting from a wider mainlobe, however, cannot be corrected due to physical limitations.

In pulse-echo, phased array systems, image lines are formed by coherently transmitting pulses to a focal point along a particular direction (i.e., beam direction $\sin\theta$) and simultaneously receiving reflected signals along the same direction using dynamically focused coherent summation. Energy is delivered mainly inside a finite lateral extent (i.e., mainlobe) determined by the aperture size and the operating frequency. A portion of the energy, however, is also delivered to directions outside the mainlobe. In other words, objects outside the beam direction are also insonified by sidelobes of the transmit beam. Therefore, these outside objects become acoustic sources. Due to sidelobes of the receive beam, such unwanted sources also contribute to the reconstruction. As the number of blocked element increases, undesired sidelobe contributions become bigger. As mentioned previously, it is the goal of blocked element compensation to estimate and remove these undesired contributions. Unfortunately, this information is "buried" in the final image since the reconstructed image is the convolution of the two way (transmit and receive) beam pattern with the reflectivity distribution in the image plane. Therefore, it is very difficult to estimate contributions from undesired sidelobes at every point given only the final image. This information, however, can be readily obtained using fixed direction transmit and dynamic (all direction) receive beamforming (i.e., multiple receive beamforming).

Multiple receive beamforming is illustrated using real measurements in figures 4 and 5. Figure 4 shows a graphite-gel heart phantom imaged with a one-dimensional, 64 element, 3.33 MHz array. Figures 4(a) and 4(b) are pulse-echo images, figures 4(c) and 4(d) are the results of fixed direction transmit and all direction receive focusing. Figures 4(a) and 4(c) are with a full array whereas figures 4(b) and 4(d) have 24 blocked elements (5-12, 17-24 and 33-40). The transmit direction is at the center. Higher sidelobes resulting from blocked elements are clearly seen in figures 4(b) and 4(d). Figure 5 shows the same processing with a different transmit direction.

With fixed direction transmit beamforming, objects at a given range are insonified and become acoustic sources. The lateral distribution of these sources sampled at the beam directions of the final image is called the true source profile $\mathbf{a}$, where each element in $\mathbf{a}$ is a complex number (i.e., strength and phase) representing an acoustic source.

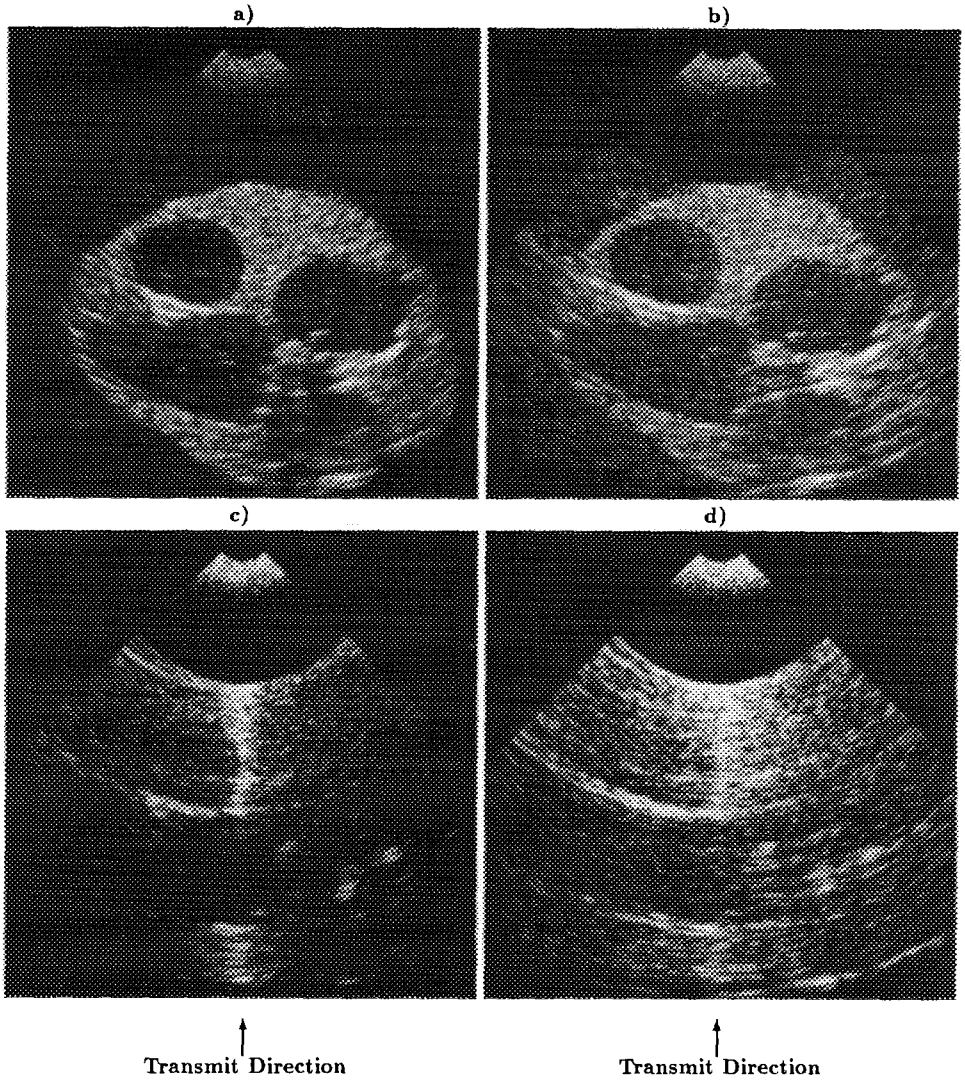

Fig. 4 Illustration of fixed direction transmit and all direction receive focusing at one transmit direction using real measurements.

With all direction receive beamforming, the true source profile is then convolved with the receive beam pattern producing a measured source profile, $\mathbf{x}$. Note that a measured source profile is simply an arc at a given range in the lower panels of figures 4 and 5. The length of $\mathbf{x}$ is equal to the number of beams in the complete sector. Hence, assuming the receive beam pattern is known, given the measured source profile ($\mathbf{x}$), the true source profile (i.e., $\mathbf{a}$) can be estimated by deconvolving $\mathbf{x}$ with the receive beam pattern. Off angle targets contributing to $\mathbf{x}$ at the primary beam direction can then be estimated and removed.

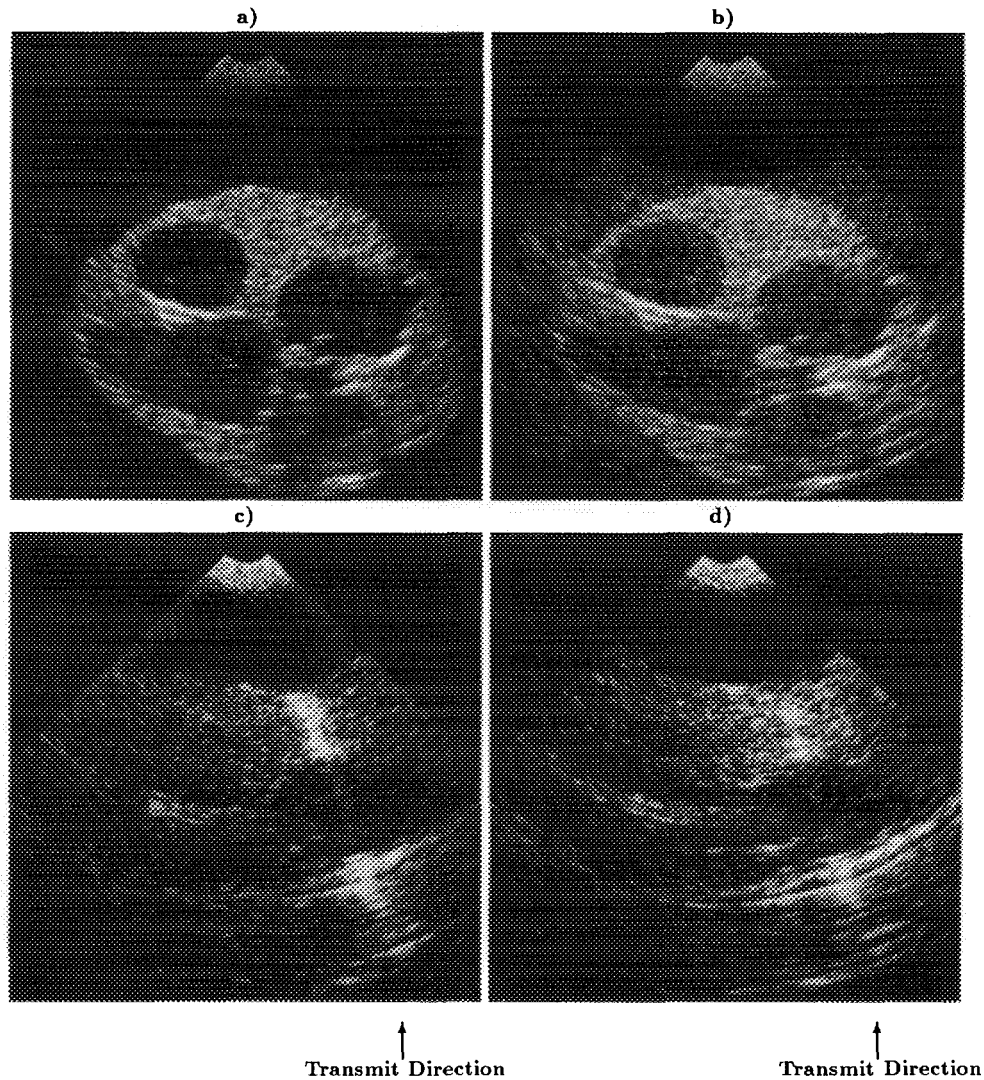

Fig. 5 Illustration of fixed direction transmit and all direction receive focusing at another transmit direction using real measurements.

The convolution relation between the true source profile (**a**) and the estimated source profile (**x**) can be represented by a set of linear equations. In other words, we have

$$\mathbf{B}\,\mathbf{a} = \mathbf{x} \quad , \tag{16}$$

where element (i, j) in **B** represents the response of the receive beam steered in a direction

i to a source in a direction j. Specifically,

$$\mathbf{B} \stackrel{def}{=} \begin{pmatrix} bp(\sin\theta_1 - \Delta_1) & bp(\sin\theta_1 - \Delta_2) & \cdots & bp(\sin\theta_1 - \Delta_m) \\ bp(\sin\theta_2 - \Delta_1) & bp(\sin\theta_2 - \Delta_2) & \cdots & bp(\sin\theta_2 - \Delta_m) \\ \vdots & \vdots & \vdots & \vdots \\ bp(\sin\theta_n - \Delta_1) & bp(\sin\theta_n - \Delta_2) & \cdots & bp(\sin\theta_n - \Delta_m) \end{pmatrix} \quad , \tag{17}$$

where $\sin\theta_i$ is the direction of the i^{th} beam line ($1 \leq i \leq n$), $bp(\sin\theta)$ is the dynamically focused receive beam pattern evaluated at direction $\sin\theta$ and Δ_j is the direction of the j-th acoustic source ($1 \leq j \leq m$). In other words, each column in $\mathbf{B}$ is a sampled receive beam pattern centered at the direction Δ_j over the entire sector. The receive patterns (i.e., $bp(\cdot)$'s) are approximated using a CW model, i.e., the Fourier transform of the receive aperture function. Therefore, columns in $\mathbf{B}$ simply represent the same ideal receive beam pattern sampled at different directions ($(\sin\theta_i - \Delta_j)$'s).

Up to this point, the problem can be stated as : *Given a measured source profile* $\mathbf{x}$, *estimate both the directions* (Δ_j*'s) and complex weighting of the true source profile* ($\mathbf{a}$). Unfortunately, it is a highly non-linear problem. To solve it, directions of acoustic sources are first estimated by finding the peak positions of the magnitude of the measured source profile. First order interpolation is also applied to improve estimation accuracy. *Note that the estimated number of acoustic sources (m, typically 3-5) is always less than the number of beam directions (n, 128 in the simulations).* Hence, it is an overdetermined problem and can be solved by least squares (LS) methods.

However, since a CW approximation is used to obtain $\mathbf{B}$, imperfection exists. Moreover, other errors such as measurement inaccuracy and model errors also exist. Therefore, rather than the traditional LS methods (where only the observation error, i.e., error in $\mathbf{x}$, is minimized), the total-least-squares (TLS) method (where the total error in both the model and observation, i.e., error in $\mathbf{B}$ and $\mathbf{x}$, is minimized) is applied. In other words, a solution to the TLS method ($\hat{\mathbf{a}}$) satisfies

$$\hat{\mathbf{B}}\hat{\mathbf{a}} \stackrel{def}{=} (\mathbf{B}+\mathbf{E})\hat{\mathbf{a}} = (\mathbf{x}+\mathbf{e}) \quad , \tag{18}$$

where $\mathbf{E}$ is the estimated model error, $\mathbf{e}$ is the estimated observation error and the Frobenius norm of the matrix $[\mathbf{E}|\mathbf{e}]$ is the total error to be minimized. Different from the ideal matrix $\mathbf{B}$, each column in $\hat{\mathbf{B}}$ represents a different beam pattern centered at an acoustic source direction since elements in $\hat{\mathbf{B}}$ are corrected independently. In other words, element (i,j) in $\hat{\mathbf{B}}$ should be denoted by $\hat{bp}_j(\sin\theta_i - \Delta_j)$.

The above formulation assumes discrete point targets. If the image point is in an anechoic region embedded in a speckle background, sidelobes from the background considerably increase its intensity and possibly create nonexisting acoustic sources in the TLS estimation. Hence, discriminating between different tissue types is necessary. A point-wise, acoustic signal-to-noise ratio (SNR), defined as the ratio of mean to standard deviation of the envelope of the scattered signal, is therefore used for this purpose. As shown in [17], the acoustic SNR's in anechoic regions obtained directly from multiple receive beams show similar trends to the SNR's obtained using larger regions. It was further shown that they are considerably higher than the value for fully developed speckle noise where the theoretical value is 1.91 for a Rayleigh distribution. Hence, in this algorithm, the acoustic SNR is calculated using multiple receive beams and the TLS method is applied if the SNR is lower than a prespecified threshold (2.5 in the simulations). The complete algorithm is summarized as follows.

At each transmit direction and reconstruction range, a set of multiple receive beams is obtained by performing fixed direction transmit and all direction receive beamforming. At each independent range, this set of beams is used to calculate the local acoustic SNR. If the SNR is higher than the threshold (e.g., 2.5), an anechoic region is assumed and therefore the pixel intensity is automatically set to zero. Otherwise, receive beams are used to estimate the true source profile iteratively. At the i-th iteration, positions of the highest i peaks are used as the directions of the strongest i acoustic sources and the TLS method is applied to find the complex strengths of these sources. The total estimation error (i.e., Frobenius norm of $[\mathbf{E}|\mathbf{e}]$) is also calculated. If the error in the i-th iteration is larger than the error in the $(i-1)$-th iteration, i.e., if a local minimum is reached at the $(i-1)$-th iteration, iteration stops and the results from the $(i-1)$-th iteration are used to correct for the CW approximation and estimate the source profile (i.e., $\hat{\mathbf{a}}$). Otherwise, the algorithm continues until a local minimum is reached. Imperfections in receive beam patterns (columns in $\mathbf{B}$) are corrected by including the estimated error $\mathbf{E}$, i.e., $\hat{\mathbf{B}} = \mathbf{B}+\mathbf{E}$.

Assuming the transmit beam direction is $\sin\theta_p$ $(1 \le p \le n)$, the estimated undesired contributions from k $(k \le m)$ off angle targets are simply

$$x_p^{undesired} = \sum_{(j \in \text{off angle region})}^{k} \hat{bp}_j(\sin\theta_p - \Delta_j)\hat{a}_j \quad , \tag{19}$$

where $\hat{a}_j$ is the complex strength of the j-th estimated source and the off angle targets are defined as the targets outside of the mainlobe of the transmit beam. Typically, the total number of sources m is about 3-5 so only a small number of contributions from k off angle targets are removed from the measured signal to produce the compensated intensity. The compensated signal along the transmit beam direction is, therefore,

$$x_p^{compensated} = x_p - x_p^{undesired} \quad . \tag{20}$$

For the details of this method, please refer to [17].

5 BLOCKED ELEMENT COMPENSATION AND CONTRAST-TO-NOISE RATIO

As described previously, the object-dependent approach utilizes multiple receive beams to estimate and remove undesired sidelobe contributions. To simulate multiple receive beamforming, the target pattern is first weighted by the transmit beam pattern centered at the transmit direction. This weighted target pattern is then convolved with the receive beam pattern to obtain multiple beams at every range for a fixed transmit direction. Given a set of multiple receive beams, the object-dependent algorithm is then applied independently for each transmit direction.

Several examples are shown. Note that for a complete simulation with blocked element compensation, the computation time is about 4 hours on a Sun SPARCstation 2. Dedicated hardware can dramatically improve this computation period. Figure 6 presents images over a 50 dB display dynamic range of an anechoic region with a 40 pixel radius (about 48 resolution cells). Figures 6(a) and 6(b) are the uncompensated images, figures 6(c) and 6(d) are the compensated images. Figures 6(a) and 6(c) are with a full array whereas figures 6(b) and 6(d) are with 16 blocked elements (17-24, 33-40). Noticeable degradation is observed in the uncompensated image with 16 blocked elements (upper right panel). With compensation, image quality is comparable to the original full

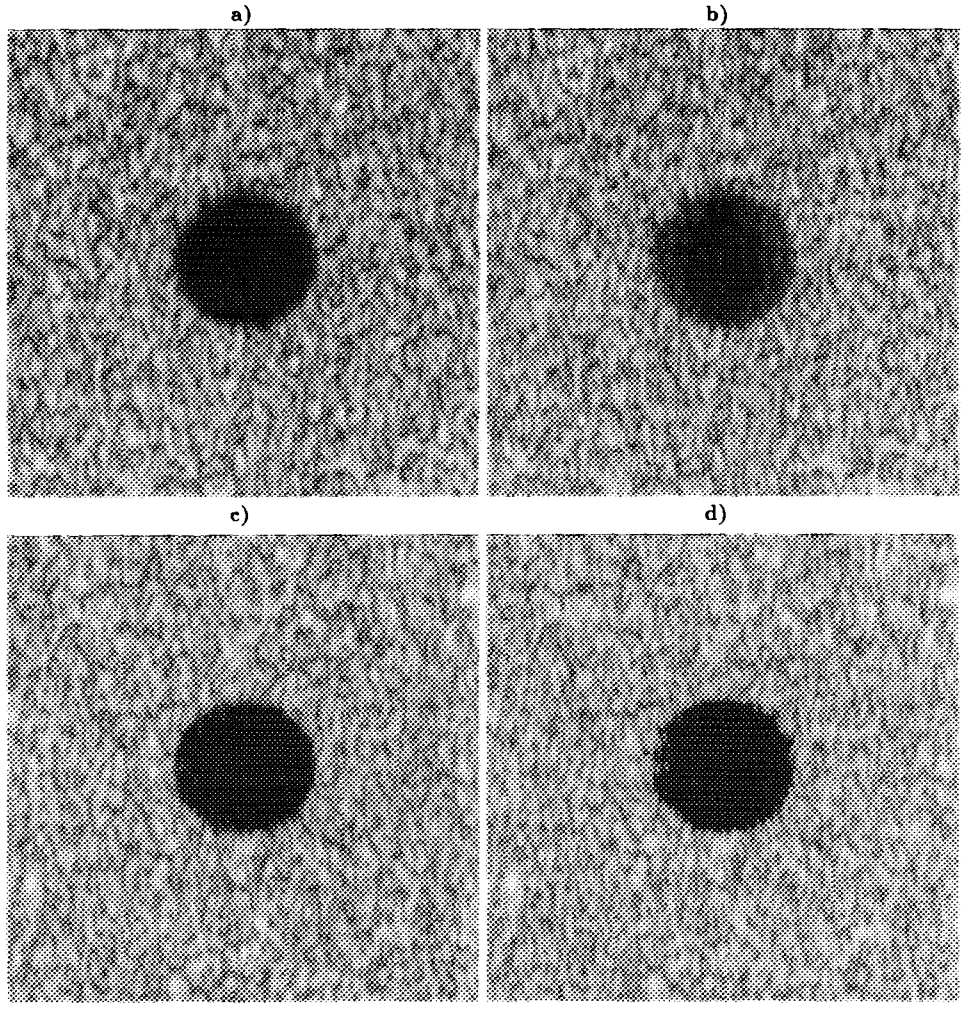

Fig. 6 Uncompensated (a and b) and compensated (c and d) images with no (a and c) and 16 (b and d) blocked elements.

array image. Even with no blocked elements, image details are still maintained with the application of the compensation algorithm (i.e., no harm is done).

Figure 7 shows the CNR as a function of the number of blocked elements, where the solid line is compensated and the dashed line is uncompensated. Roughly, the CNR decreases as a function of the number of blocked elements without compensation. The primary source of degradation is the convolution of sidelobes with the background. With compensation, the CNR is maintained if the number of blocked elements is not very significant (16 out of 64). If the number is large, the method breaks down and the difference between with and without compensation becomes smaller. In general, the

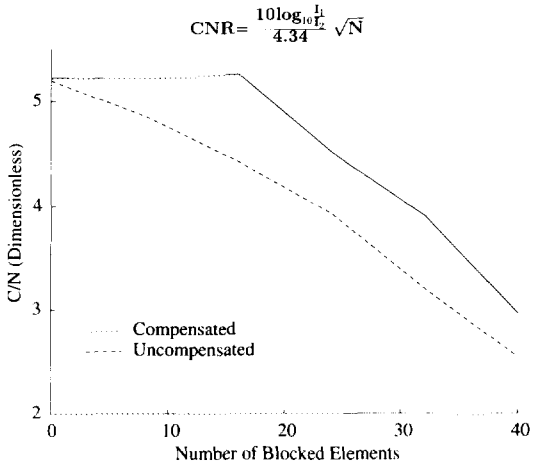

Fig. 7 CNR as a function of the number of blocked elements.

algorithm provides a fixed 0.5 CNR improvement for this example if the number of blocked elements is very significant.

Figure 8 shows images of a target pattern with a 20 pixel radius (about 12 resolution cells) but only a 10 dB contrast (the disk is 10 dB lower than the background). Figures 8(a) and 8(b) are the uncompensated images, figures 8(c) and 8(d) are the compensated images. Figures 8(a) and 8(c) are with a full array whereas figures 8(b) and 8(d) are with 24 blocked elements (5-12, 17-24 and 33-40). All images use a 30 dB display dynamic range. Since both the target and the background have Rayleigh statistics, the compensation algorithm is applied without using a statistical analysis to discriminate tissue types. Although differences are not pronounced for the low contrast example, degradation is still discernible in the upper right panel. With compensation, the target is more observable.

Figure 9 shows the CNR as a function of the number of blocked elements, where again the solid line shows the compensated results and the dashed line uncompensated results. Because of the low contrast (10 dB) between the target and the background and the small size of the target, the CNR's of the uncompensated images do not decrease with the same slope as observed in figure 7. With compensation, the CNR can be improved even in the presence of a significant number of blocked elements. The difference between with and without compensation is very small if a large number of blocked elements is present.

6 CONCLUDING REMARKS

In a previous paper, we have introduced compensation methods and shown that image quality can be greatly improved in the presence of blocked elements. In this paper, we further study the factors of detectability using area-wise speckle statistics and quantify the improvement with the compensation method. In the examples shown in this paper, detectability can be fully recovered even with 25% of the elements missing. In most

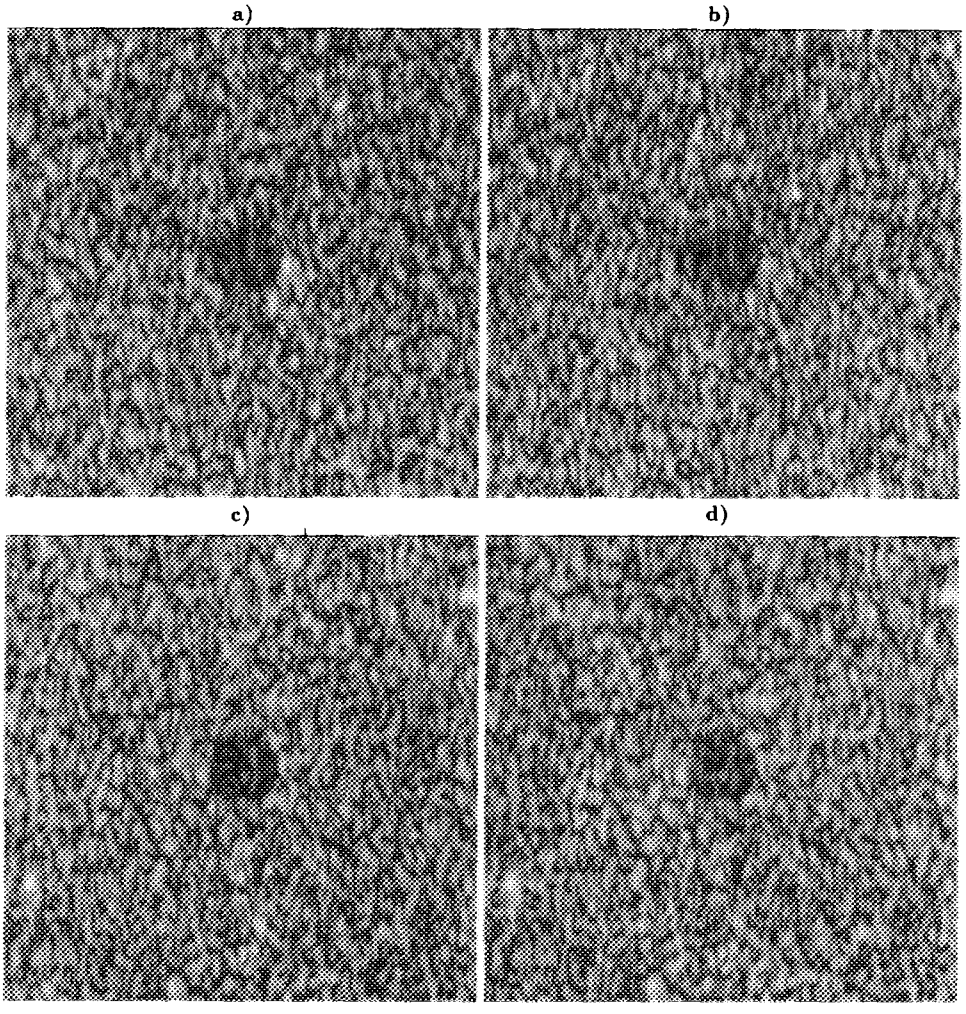

Fig. 8 Uncompensated (a and b) and compensated (c and d) images with no (a and c) and 24 (b and d) blocked elements.

clinical situations, this method may play an essential role in fully realizing the potential of VLA's.

As noted by other authors, we have also shown that contrast resolution is determined mainly by the number of independent speckles and the sidelobe energy. If total aperture size is not reduced, the number of independent speckles does not change and sidelobes dominate low contrast detectability. With the application of an object dependent compensation algorithm, sidelobe artifacts can be greatly reduced and therefore the CNR can be improved if the number of blocked elements is not very significant. If the number of blocked elements is large, however, the algorithm breaks down due to physical limitations.

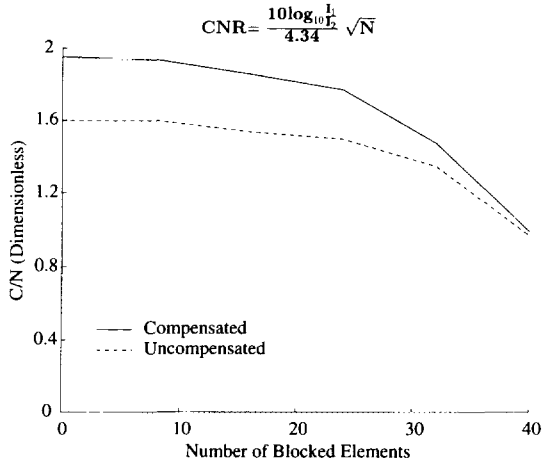

Fig. 9 CNR as a function of the number of blocked elements.

Fundamental differences are observed between high contrast results (Fig. 7) and low contrast results (Fig. 9). Undesired sidelobes can be well removed using statistical analysis in the high contrast case since the statistics are very different between the background and lesion. This explains why the compensated CNR's can be maintained in figure 9 if the number of blocked elements is not very significant (16 out of 64). In low contrast cases, however, it is difficult to distinguish weak mainlobes in the lesions and high sidelobes from the background. Hence, improvement is limited. On the other hand, increased brightness in the lesion comes solely from the background in high contrast situations. It is therefore linearly proportional to the number of blocked elements on a logarithmic scale. In low contrast cases, background contributions are relatively lower than mainlobe signals within the lesion, thus producing a slowly decreasing curve in CNR.

Finally, note that this paper mainly addresses compensation in the azimuthal direction. With two-dimensional arrays, the algorithm must also be applied in elevation. Depending on array geometries, the capability of steering beams in the elevational direction also varies. Unlike fully sampled arrays, anisotropic arrays steer over limited angles in elevation. Hence, the performance of compensation in this direction might be slightly degraded. Further studies will explore methods that compensate for blocked element degradation in elevation.

ACKNOWLEDGMENTS

Support supplied by the National Institutes of Health under Grant CA 54896 and by the General Electric Company is gratefully acknowledged. The authors thank the reviewers and Wayne Rigby of General Electric for helpful comments. The authors would also like to thank Mark Lubinski, Stas Emelianov and Steve Freeman for help in the final production of the paper.

REFERENCES

[1] Smith, S.W. and Lopez, H, A contrast detail analysis of diagnostic ultrasound imaging, *Med. Phys. 9*, 4-12 (1982).

[2] Burckhardt, C.B., Speckle in ultrasound B-mode scans, *IEEE Trans. Sonics Ultrason. 25*, 1-6 (1978).

[3] Trahey, G.E., Smith, S.W. and von Ramm, O.T., Speckle pattern correlation with lateral aperture translation: experimental results and implications for spatial compounding, *IEEE Trans. Ultrason., Ferroelec., Freq. Contr. 33*, 257-264 (1986).

[4] Silverstein, S.D., and O'Donnell, M., Frequency and Temporal Compounding of Partially Correlated Signals: Speckle Suppression and Image Resolution, in *SPIE 845 Visual Communications and Image Processing II*, pp. 188-194 (SPIE, Bellingham, 1987).

[5] O'Donnell, M., and Silverstein, S.D., Optimum displacement for compound image generation in medical ultrasound, *IEEE Trans. Ultrason, Ferroelec., Freq. Contr. 35*, 470-476 (1988).

[6] Trahey, G.E., Allison, J.W., Smith, S.W. and von Ramm, O.T., Speckle Pattern Changes with Varying Acoustic Frequency: Experimental Measurement and Implications for Frequency Compounding, in *Proc. of the 1986 IEEE Ultrasonics Symposium*, pp. 815-818, IEEE Cat. No. 86CH2375-4 (IEEE, New York, 1986).

[7] Sheikh, K.H., Smith, S.W., von Ramm, O.T. and Kisslo, J., Real-time, three-dimensional echocardiography: feasibility and initial use, *Echocardiography 8*, 199-225 (1991).

[8] Smith, S.W., Trahey, G.E. and von Ramm, O.T., Two-dimensional arrays for medical ultrasound, *Ultrasonic Imaging, 14*, 213-233 (1992).

[9] Turnbull, D.H., Kerr, A.T. and Foster, F.S., Simulation of B-scan Images from Two-dimensional Transducer Arrays, in *Proceedings of the 1990 IEEE Ultrasonics Symposium*, pp. 769-773, IEEE Cat. No. 90CH2938-9 (IEEE, New York, 1990).

[10] O'Donnell, M. and Li, P.-C., Aberration Correction on a Two-dimensional Anisotropic Phased Array, in *Proceedings of the 1991 IEEE Ultrasonics Symposium*, pp. 1189-1193, IEEE Cat. No. 91CH3079-1 (IEEE, New York, 1991).

[11] Hirama, M. and Sato, T, Imaging through an inhomogeneous layer by least-mean-square error fitting, *J. Acoust. Soc. Am., 75* 1142-1147 (1984).

[12] Flax, S.W. and O'Donnell, M., Phase aberration correction using signals from point reflectors and diffuse scatterers: Basic principles, *IEEE Trans. Ultrason., Ferroelec. Freq. Contr. 35*, 758-767 (1988).

[13] O'Donnell, M. and Flax, S.W., Phase aberration correction using signals from point reflectors and diffuse scatterers: Measurement, *IEEE Trans. Ultrason., Ferroelec. Freq. Contr. 35*, 768-774 (1988).

[14] Nock, L., Trahey, G.E. and Smith, S.W., Phase aberration correction in medical ultrasound using speckle brightness as a quality factor, *J. Acoust. Soc. Am., 85*, 1819-1833 (1988).

[15] Rachlin, D., Direct estimation of aberrating delays in pulse-echo imaging systems, *J. Acoust. Soc. Am., 88*, 191-198 (1990).

[16] Zhu, Q. and Steinberg, D., Large transducer measurements of wavefront distortion in the female breast, *Ultrasonic Imaging, 14*, 276-299 (1992).

[17] Li, P.-C., Flax, S.W., Ebbini, E.S. and O'Donnell, M., Blocked element compensation in phased array imaging, *IEEE Trans. Ultrason., Ferroelec. Freq. Contr. 40*, 283-292 (1993).

[18] Macovski, A., *Medical Imaging Systems* (Prentice-Hall, Englewood Cliffs, 1983).

[19] Goodman, J.W., Statistical Properties of Laser Speckle Patterns, in *Laser Speckle and Related Phenomena* (Springer-Verlag, Berlin, 1975).

[20] Wagner, R.F., Smith, S.W., Sandrik, J.M. and Lopez, H, Statistics of speckle in ultrasound B-scans, *IEEE Trans. Sonics Ultrason. 30*, 156-163 (1983).

[21] Smith, S.W., Wagner, R.F., Sandrik, J.M. and Lopez, H., Low contrast detectability and contrast/detail analysis in medical ultrasound, *IEEE Trans. Sonics Ultrason. 30*, 164-173 (1983).

[22] Smith, S.W. and Wagner, R.F., Ultrasound speckle size and lesion signal to noise ratio: verification of theory, *Ultrasonic Imaging, 6*, 174-180 (1984).

[23] Wagner, R.F., Insana, M.F. and Smith, S.W., Fundamental correlation lengths of coherent speckle in medical ultrasonic images, *IEEE Trans. Ultrason., Ferroelec. Freq. Contr. 35*, 34-44 (1988).

[24] Edelstein, W.A., Bottomley, P.A., Hart, H.R. and Smith, L.S., Signal, noise, and contrast in nuclear magnetic resonance (NMR) imaging, *J. Computer Assisted Tomog. 7*, 391-401 (1983).

[25] Meyer, P.L., *Introductory Probability and Statistical Applications* (Addison-Wesley, Reading, 1970).